Li, Penglei et al.

Article

Entropy generation rate minimization for steam methane reforming reactor heated by molten salt

Energy Reports

Provided in Cooperation with:
Elsevier

Suggested Citation: Li, Penglei et al. (2020) : Entropy generation rate minimization for steam methane reforming reactor heated by molten salt, Energy Reports, ISSN 2352-4847, Elsevier, Amsterdam, Vol. 6, pp. 685-697, https://doi.org/10.1016/j.egyr.2020.03.011

This Version is available at:
https://hdl.handle.net/10419/244068

Energy Reports 6 (2020) 685–697

Contents lists available at ScienceDirect

Energy Reports

journal homepage: www.elsevier.com/locate/egyr

Research paper

Entropy generation rate minimization for steam methane reforming reactor heated by molten salt

Penglei Li [a,b,c], Lingen Chen [a,b,*], Shaojun Xia [c], Lei Zhang [a,b,c], Rui Kong [a,b,c], Yanlin Ge [a,b], Huijun Feng [a,b,c]

[a] Institute of Thermal Science and Power Engineering, Wuhan Institute of Technology, Wuhan 430205, PR China
[b] School of Mechanical & Electrical Engineering, Wuhan Institute of Technology, Wuhan 430205, PR China
[c] College of Power Engineering, Naval University of Engineering, Wuhan 430033, PR China

ARTICLE INFO

Article history:
Received 27 December 2019
Received in revised form 28 February 2020
Accepted 10 March 2020
Available online xxxx

Keywords:
Steam methane reforming
Molten salt
Minimum entropy generation rate
Finite-time thermodynamics
Hybrid particle swarm optimization

ABSTRACT

Traditional steam methane reforming facilities for producing hydrogen not only consume a large amount of natural gas, but also emit a lot of greenhouse gas. Considering the utilization of clean energy, the reduction of carbon dioxide emission, and the production of chemicals, this paper establishes a model of steam methane reforming reactor heated by molten salt by utilizing finite-time thermodynamics. In order to reduce the irreversibility of this reactor, the entropy generation rate minimization and some operating parameters are taken as the optimization objective and variables, respectively. The hybrid particle swarm optimization algorithm is proposed for solving this model. Afterwards, the influences of the porosity of the catalyst bed and catalyst activity on the optimal performance are analyzed. The results indicate that the total entropy generation rate of the reactor is reduced by 22.08% after optimizing the inlet parameters of the molten salt and reaction mixture. Within the scope of this study, the total entropy generation rate of the optimal reactor decreases with the increasing porosity of catalyst bed. When the catalyst activity decreases, the hydrogen production rate can remain constant by adjusting the operating parameters. The obtained results are favorable to guide the optimal design of the practical reactors.

1. Introduction

Although the traditional rugged development brings huge economic benefits to the world, it has elicited a lot of problems, such as resource waste, environment pollution, and the greenhouse effect (Saidi and Hammami, 2015). At present, ecological environment protection and sustainable development have become the focus problem (Albassam et al., 2018; Chaubey et al., 2013). Hydrogen has attracted much attention due to its clean and renewable. So far, the technical routes for hydrogen production mainly include the water electrolysis, the steam methane reforming (SMR) (Pashchenko, 2019a), the chemical looping steam reforming (Guo et al., 2016), the dry reforming of methane (Blooma et al., 2018), the biomass and photovoltaic. Among them, the SMR is widely used technical route for hydrogen production. In fact, the SMR can also be used to produce the synthesis gas, it is widely used in various industries (Pashchenko, 2019c,b). Therefore, analyzing the traditional SMR process by using various analysis methods and improving it by utilizing the novel technology own more practical significance, in the short term (Boyano et al., 2011; Hajjaji et al., 2012).

Hajjaji et al. (2012), Simpson and Lutz (2007), Boyano et al. (2012), and Chen et al. (2012) analyzed the traditional SMR process by using the exergy analysis and advanced exergy analysis, and proposed the improvement schemes for the process generating abundant destroyed exergy. To reduce the destroyed exergy and the greenhouse gas emissions, Falco et al. (2014b) and Diglio et al. (2017) combined the technology of hydrogen permeation membrane and the carbon dioxide adsorption with the traditional SMR process, respectively. Many researchers used solar energy (Falco et al., 2014a; Jin et al., 2018), nuclear energy (Hoseinzade and Adams, 2017), and high-temperature flue gas from the solid oxide fuel cell (Sciazko et al., 2014) as the alternatives of the methane combustion. Among them, the solar steam reforming technology holds bright prospects, because of its green, clean and renewable.

Giaconia et al. (2008) proposed three SMR processes integrated with the molten salt (MS), which is heated by the solar radiation, and analyzed those processes by utilizing AspenPlus. Piemonte et al. (2012) utilized the LCA software (Simapro7) to

* Corresponding author at: Institute of Thermal Science and Power Engineering, Wuhan Institute of Technology, Wuhan 430205, PR China.
E-mail addresses: lgchenna@yahoo.com, lingenchen@hotmail.com (L. Chen), 398843013@qq.com (S. Xia).

https://doi.org/10.1016/j.egyr.2020.03.011

Nomenclature

A	Cross sectional area, m^2
c	Superficial velocity, m s^{-1}
C_P	Molar heat capacity at constant pressure, J mol^{-1} K^{-1}
d	Diameter, m
D	Hydraulic diameter, m
F	Molar flow rate, mol s^{-1}
h	Convective heat transfer coefficient, W m^{-2} K^{-1}
P	Pressure, bar
r	Reaction rate, mol s^{-1} kg^{-1}
Sg	Entropy generate rate, W K^{-1}
T	Temperature, K
z	Axial coordinate

Greek symbols

ε	Porosity
η	Intraparticle diffusion effective factors
λ	Thermal conductivity, W m^{-1} K^{-1}
μ	Viscosity, kg m^{-1} s^{-1}
σ	Local entropy generate rate, W K^{-1} m^{-1}

Subscripts

B	Catalyst bed
C	Catalyst particle
i	Reaction i
k	Component k
MS	Molten salt
Ri	Internal of the reactor
Ro	External of the reactor
RM	Reaction mixture

Abbreviations

CB	Catalyst bed
EGR	Entropy generation rate
HPR	Hydrogen production rate
HT	Heat transfer
MFR	Molar flow rate
MS	Molten salt
MS-SMR	Steam methane reforming reactor heated by molten salt
RM	Reaction mixture
RT	Reactor tube
SMR	Steam methane reforming reactor

make the life cycle assess to the facilities in the above processes. Falco et al. (2014a) established a two-dimensional steam methane reforming reactor heated by the MS (MS-SMR) model, and analyzed the influences of the space velocity, temperature of the reaction mixture (RM), and reactor length on the methane conversion rate. The studies mentioned above for the MS-SMR reactors did not consider the parameter optimization. Therefore, advanced thermodynamic theory is needed to optimize the MS-SMR reactor.

Finite-time thermodynamics (Andresen et al., 1984; Chen et al., 1999; Andresen, 2011) uses optimal control theory and optimization algorithm to study various irreversible processes and cycles, and obtains many meaningful results to guide the designs of the practical equipments, including chemical syntheses (Schön, 2009), internal combustion engine (Ge et al., 2016), steady state optimization of various processes and cycles (Chen and Sun, 2004; Chen, 2005), dynamic-optimizations of irreversible processes (Chen and Xia, 2017, 2019) and cycles (Chen and Xia, 2018a,b; Chen et al., 2019), biological processes (Roach et al., 2018), organic Rankine cycle (Abam et al., 2018), sustainable development (Lucia and Grisolia, 2019), heat and power cogeneration plant (Feng et al., 2019), fuel cell combined system Açıkkalp et al. (2020), etc. In the engineering, it is also called the entropy generation minimization (Bejan, 1982, 1996b,c,a, 2013) or thermodynamic optimization, which is the method of modeling and optimization of real devices that owe their thermodynamic imperfection to heat transfer, mass transfer, and fluid flow irreversibilities (Bejan, 1996b).

In solving the optimization problems of chemical industrial, chemical engineers generally tend to pursue the maximum target production rate (Månsson and Andressen, 1986; Piña et al., 2001; Pantoleontos et al., 2012; Li et al., 2019b; Wang et al., 2016), while thermodynamic researchers tend to improve the energy efficiency at a fixed target production rate, which is consistent with decreasing the exergy loss (Leites et al., 2003). According to the Gouy–Stodola theory, the exergy loss is equal to the product of the entropy generation and the ambient temperature. Therefore, the entropy generation rate (EGR) minimization at a fixed target production rate can be used to decrease the irreversibilities of the chemical reactor, and to improve its energy efficiency. Taking the EGR minimization as the optimization objective, the team of Kjelstrup optimized the methanol synthesis via carbon dioxide hydrogenation reactor (Kjelstrup et al., 2000), the ammonia synthesis reactor (Nummedal et al., 2003), the SO_2 oxidation reactor (Johannessen and Kjelstrup, 2004), and the SMR reactor (Nummedal et al., 2005; Wilhelmsen et al., 2010). The team of Chen (Ao et al., 2018; Chen et al., 2018a; Zhang et al., 2018, 2020; Li et al., 2019a; Chen et al., 2018b; Zhang et al., 2019) optimized the SMR reactor (Ao et al., 2018; Chen et al., 2018a), the reverse water gas shift reactor (Zhang et al., 2018, 2020), the methanol synthesis via carbon dioxide hydrogenation reactor (Li et al., 2019a), and the carbon dioxide hydrogenation to light olefins reactor (Chen et al., 2018b; Zhang et al., 2019). Kingston and Razzitte (2017, 2018) applied EGR minimization to ideal reactors and practical industrial reactors, analyzed thermodynamic performance of the stirred tank and plug flow reactors (Kingston and Razzitte, 2017), and obtained the optimal parameters to the dimethyl ether synthesis reactor (Kingston and Razzitte, 2018).

The purpose of this paper is to reduce the total EGR, which consists of the EGRs caused by the heat transfer process of the finite temperature difference, the chemical reaction processes of the finite reaction rates, and the viscous flow process of the finite pressure drop, under the fixed hydrogen production rate (HPR) by adjusting the operating parameters of the MS-SMR reactor. Firstly, a one-dimensional MS-SMR reactor, which includes the annular heating tube model, the complex heat transfer model and some empirical formulas to describe some thermodynamic parameters, is established based on FTT theory. Then, the optimal operating parameters of the MS-SMR reactor are obtained by using the proposed hybrid particle swarm optimization algorithm. Afterwards, the performance of the optimal reactor is analyzed. Finally, the influences of the porosity of the catalyst bed (CB) and the catalyst activity on the optimization results are analyzed.

2. System description and reactor model

2.1. System description

Xu and Froment (1989b,a) studied the mechanism of the SMR reaction catalyzed by $Ni/MgAl_2O_4$, and proposed the detailed

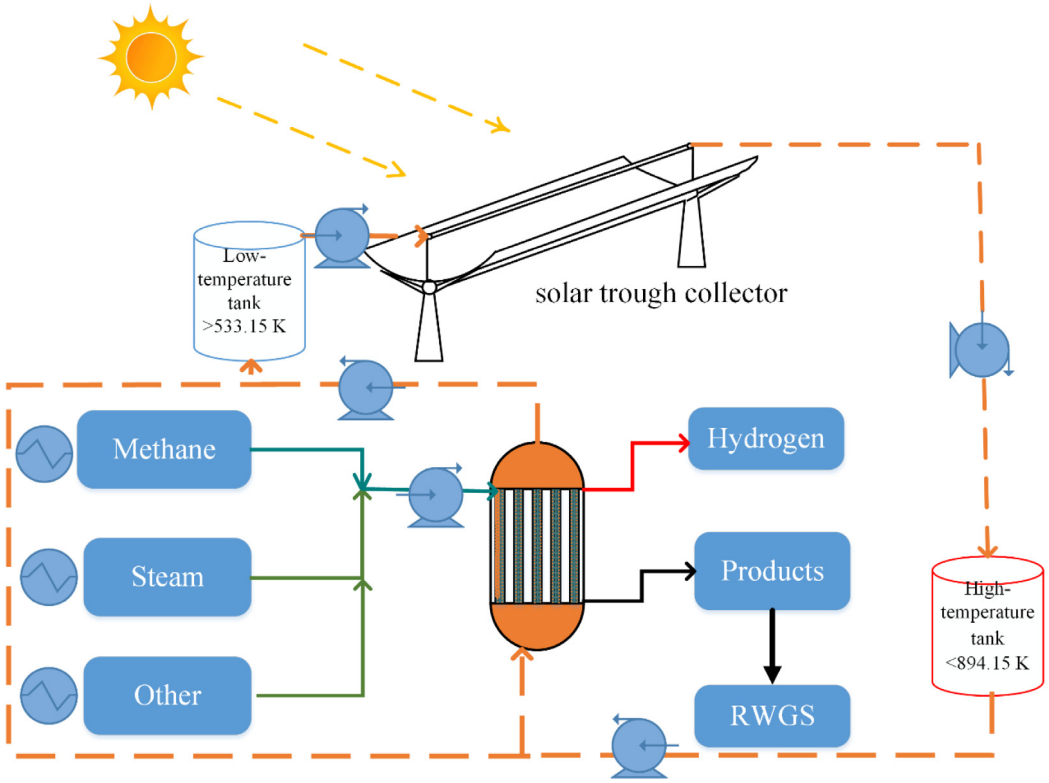

Fig. 1. Schematic diagram of the hydrogen production process based on the MS-SMR reactor.

reaction kinetic model for three main reactions:

$$CH_4 + H_2O \rightleftharpoons CO + 3H_2 \qquad \Delta_r H_1 > 0 \tag{1}$$

$$CO + H_2O \rightleftharpoons CO_2 + H_2 \qquad \Delta_r H_2 < 0 \tag{2}$$

$$CH_4 + 2H_2O \rightleftharpoons CO_2 + 4H_2 \qquad \Delta_r H_3 > 0 \tag{3}$$

where $\Delta_r H_i$ denotes the reaction enthalpy of each reaction, which can be calculated by using the empirical formulas in Appendix A.

The schematic diagram of the MS-SMR process for hydrogen production is shown in Fig. 1, which mainly includes three parts, i.e. the solar trough collector section (Alotaibi et al., 2020), two tanks for MS storage, and the SMR reactor (Albassam et al., 2018; Giaconia et al., 2008). The high-temperature MS, heated by the solar radiation in the solar trough collector, is stored in an insulated high-temperature tank to be pumped, afterwards to the SMR reactor, where it heats the RM. Afterwards, the MS is pumped to an insulated lower-temperature tank, and then return to the solar trough collector (Giaconia et al., 2008). As shown in Fig. 1, Many reactor tubes (RT) are placed vertically inside the reactor furnace, where the MS releases the sensible heat to the RM. These RTs have similar geometric and physical characteristics, therefore, one such TR is selected as the research object. Pashchenko (2018) investigated the effect of geometric dimensionality on the simulation results of the steam methane reforming reactor, the results indicated that the results for one-dimensional, two-dimensional and three-dimensional models almost similar, when the residence time is more than 8 and the relative length is more than 15. The residence time and the relative length in this paper are 8.7 and 200, respectively. Therefore, a one-dimensional reactor model, which consists of the RT filled with catalyst particles and the annular heating tube filled with the MS, is established shown in Fig. 2.

Chemical reactor contains multiple transfer phenomena. If all transfer phenomena been factored in, solving and optimizing the reactor becomes very difficult. In order to facilitate solving the proposed model in this paper, some assumptions are considered:

(1) No back mixing of the RM exists in the axial direction. This assumption is reasonable, because the ratio of reactor length L and equivalent diameter of the catalyst particles d_C is greater than 150.

(2) The RT is assumed as the plug flow pattern, because the aspect ratio of the reactor L/d_{Ri} is greater than 100.

(3) The RM is processed as the ideal gas, since the operating pressure is not too high (Pantoleontos et al., 2012; Nummedal et al., 2005).

(4) The pressure drop in the annular heating tube is ignored.

(5) The outer wall of the annular heating tube is assumed to be adiabatic.

2.2. Reactor tube model

The axial temperature of the RM T_{RM} is written as follows (Wesenberg, 2006)

$$\frac{dT_{RM}}{dz} = \frac{\pi d_{Ri} J_q - \rho_C A_{Ri} (1-\varepsilon_B) \cdot \sum_{i=1}^{3} (\eta_i r_i \Delta_r H_i)}{\sum_{k=1}^{6} F_k C_{P,k}} \tag{4}$$

where d_{Ri} denotes the inner diameter of the RT, J_q denotes the heat flux through the wall of the reactor tube, ρ_C denotes the apparent density of the catalyst particles, A_{Ri} denotes the cross sectional area of the RT, ε_B denotes the porosity of the CB, η_i, and r_i denote the intraparticle diffusion efficiency factor, and intrinsic reaction rate of each reaction, respectively, F_k and $C_{P,k}$ denotes the molar flow rate (MFR) and molar heat capacity of component k, and $C_{P,k}$ is calculated by using the empirical formulas in Appendix A.

Re_C is the Reynolds number for fixed bed. For $Re_C/(1-\varepsilon_B) \approx$ 5000, the pressure drop is described by using Hicks equation as

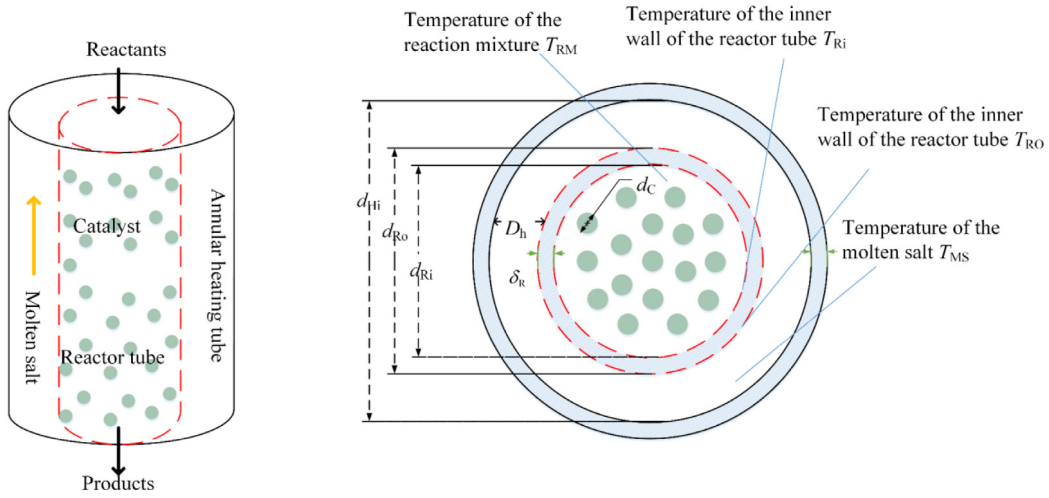

Fig. 2. One-dimensional pseudo-homogeneous plug flow reactor model.

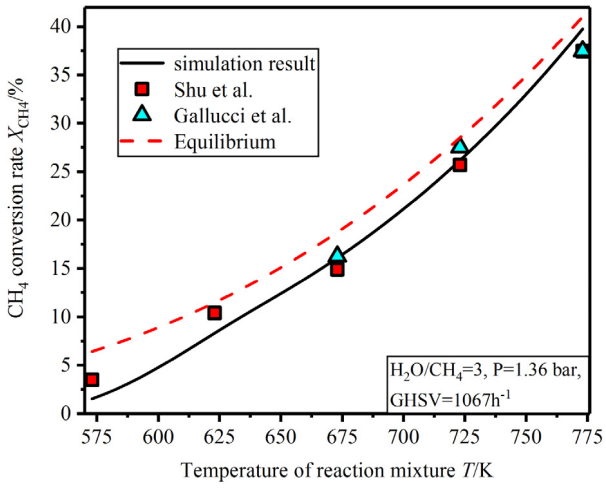

Fig. 3. The CH_4 conversion rate versus the temperature of the RM under the simulation, thermodynamic equilibrium and experimental.

follows (Hicks, 1970)

$$\frac{dP_{RM}}{dz} = -6.8\frac{(1-\varepsilon_B)^{1.2}}{\varepsilon_B^3} Re_C^{-0.2}\frac{\rho_{RM}c_{RM}^2}{d_C}$$

$$\text{s.t. } 300 < \frac{Re_C}{1-\varepsilon_B} < 60000 \tag{5}$$

where ρ_{RM} and c_{RM} denote the density and superficial velocity of the RM, respectively.

The MFRs of components are described by using the molar mass conservation equation as follows:

$$\frac{dF_{CH_4}}{dz} = -\rho_C A_{Ri}(1-\varepsilon_B)\cdot(\eta_1 r_1 + \eta_3 r_3) \tag{6}$$

$$\frac{dF_{H_2O}}{dz} = -\rho_C A_{Ri}(1-\varepsilon_B)\cdot(\eta_1 r_1 + \eta_2 r_2 + \eta_3 r_3) \tag{7}$$

$$\frac{dF_{H_2}}{dz} = \rho_C A_{Ri}(1-\varepsilon_B)\cdot(3\eta_1 r_1 + \eta_2 r_2 + \eta_3 r_3) \tag{8}$$

$$\frac{dF_{CO}}{dz} = \rho_C A_{Ri}(1-\varepsilon_B)\cdot(\eta_1 r_1 - \eta_2 r_2) \tag{9}$$

$$\frac{dF_{CO_2}}{dz} = \rho_C A_{Ri}(1-\varepsilon_B)\cdot(\eta_2 r_2 + \eta_3 r_3) \tag{10}$$

2.3. Annular heating tube model

The annular heating tube is filled with the MS, which is composed of 60% $NaNO_3$ and 40% KNO_3 (Zavoico, 2001). It is known as "solar salt", because of its high heat capacity, stable property and less volatile. The axial temperature of the MS T_{MS} is written as follows (Nummedal et al., 2005; Zhang et al., 2020):

$$\frac{dT_{MS}}{dz} = \frac{\pi \cdot d_{Ri}\cdot J_q}{F_{MS}C_{P,MS}} \tag{11}$$

where F_{MS} denote the MFR of the MS, and the heat capacity of the MS $C_{P,MS}$ is calculated by using the empirical formula in Appendix A.

2.4. Heat transfer model

The energy conservation equations in the outer and inner walls of the RT are, respectively, as follows (Yang and Tao, 2006):

$$h_{MS}^{Ro}(T_{MS} - T_{Ro}) = \frac{2\lambda_R(T_{Ro} - T_{Ri})}{d_{Ro}\ln(d_{Ro}/d_{Ri})} \tag{12}$$

$$h_{RM}^{Ri}(T_{Ri} - T_{RM}) = \frac{2\lambda_R(T_{Ro} - T_{Ri})}{d_{Ri}\ln(d_{Ro}/d_{Ri})} \tag{13}$$

where T_{Ri} and T_{Ro} denote the temperature of the inner and outer walls in the RT, respectively, d_{Ro} denotes the outer diameter of the RT, and the convection coefficients h_{MS}^{Ro} and h_{RM}^{Ri} are calculated by using the empirical formulas in Appendix B.

The heat flux is written as follows (Yang and Tao, 2006)

$$J_q = h_{RM}^{Ri}(T_{Ri} - T_{RM}) \tag{14}$$

2.5. Reaction kinetic model

Xu and Froment (1989b,a) established the reaction kinetic model for the SMR reaction catalyzed by $Ni/MgAl_2O_4$. This model has been widely used in the researches on the SMR reactor (Pantoleontos et al., 2012; Li et al., 2019b; Wang et al., 2016; Nummedal et al., 2005; Wilhelmsen et al., 2010; Ao et al., 2018; Chen et al., 2018a). The intrinsic reaction rates are written as follows:

$$r_1 = \alpha\frac{k_1}{3.6\cdot P_{H_2}^{2.5}DEN^2}\left(P_{CH_4}P_{H_2O} - \frac{P_{H_2}^3 P_{CO}}{K_1}\right) \tag{15}$$

$$r_2 = \alpha\frac{k_2}{3.6\cdot P_{H_2}DEN^2}\left(P_{CO}P_{H_2O} - \frac{P_{H_2}P_{CO_2}}{K_2}\right) \tag{16}$$

Table 1
The local EGR of the mainly irreversible processes in the reactor[a].

Local EGR	Expression	Local EGR	Expression
$\sigma_{\mathrm{H,MS\text{-}Ro}}$	$\pi \cdot d_{\mathrm{Ri}} J_q \cdot [(1/T_{\mathrm{Ro}}) - (1/T_{\mathrm{MS}})]$	σ_P	$A_{\mathrm{Ri}} c_{\mathrm{RM}} \frac{1}{T_{\mathrm{RM}}} \frac{\mathrm{d}P_{\mathrm{RM}}}{\mathrm{d}z}$
$\sigma_{\mathrm{H,Ro\text{-}Ri}}$	$\pi \cdot d_{\mathrm{Ri}} J_q \cdot [(1/T_{\mathrm{Ri}}) - (1/T_{\mathrm{Ro}})]$	σ_{r_i}	$-\rho_{\mathrm{C}} (1-\varepsilon_{\mathrm{B}}) A_{\mathrm{Ri}} \eta_i r_i \left(\frac{\Delta_r G_i}{T_{\mathrm{RM}}}\right)$
$\sigma_{\mathrm{H,Ri\text{-}RM}}$	$\pi \cdot d_{\mathrm{Ri}} J_q \cdot [(1/T_{\mathrm{RM}}) - (1/T_{\mathrm{Ri}})]$	σ_{H}	$\pi \cdot d_{\mathrm{Ri}} J_q \cdot [(1/T_{\mathrm{RM}}) - (1/T_{\mathrm{MS}})]$

[a]Where σ_{H} denotes the local EGR attributed to all HT processes, $\Delta_r G_i$ denotes the Gibbs free energy of each reaction (Bejan, 1996a; Wang et al., 2016).

Table 2
Parameters setting of the reference reactor.

Parameters	Symbol	Value (unit)
Geometric parameters		
Inner diameter of the annular heating tube	d_{Hi}	0.200 m
Hydraulic diameter of the annular heating tube	D_{h}	0.090 m
Inner diameter of the RT	d_{Ri}	0.110 m
Outer diameter of the RT	d_{Ro}	0.134 m
Wall thickness of the RT	δ_{R}	0.012 m
Heat conductivity of the RT wall	λ_{R}	50 W m^{-1} K^{-1}
Mole fraction of the inlet composition		
Methane and steam	y^0_{SM}	0.9273
Hydrogen	$y^0_{\mathrm{H_2}}$	0.0260
Carbon dioxide	$y^0_{\mathrm{CO_2}}$	0.0119
Nitrogen	$y^0_{\mathrm{N_2}}$	0.0349
Parameters of the catalyst Ni/$MgAl_2O_4$		
Particle diameter	d_{C}	7.265 × 10^{-3} m
Particle density	ρ_{C}	2355.2 kg m^{-3}
Heat conductivity of the particle	λ_{C}	0.3489 W m^{-1} K^{-1}
Tortuosity factor	τ	3.54
Particle porosity	ε_{C}	0.59
Porosity of the CB	ε_{B}	0.65
Catalyst activity	α	1
Particle emissivity	$\varepsilon_{\mathrm{em}}$	0.8

$$r_3 = \alpha \frac{k_3}{3.6 \cdot P_{\mathrm{H_2}}^{3.5} DEN^2} \left(P_{\mathrm{CH_4}} P_{\mathrm{H_2O}}^2 - \frac{P_{\mathrm{H_2}}^4 P_{\mathrm{CO_2}}}{K_3} \right) \tag{17}$$

$$DEN = 1 + K_{\mathrm{CO}} P_{\mathrm{CO}} + K_{\mathrm{H_2}} P_{\mathrm{H_2}} + K_{\mathrm{CH_4}} P_{\mathrm{CH_4}} + (K_{\mathrm{H_2O}} P_{\mathrm{H_2O}})/P_{\mathrm{H_2}} \tag{18}$$

where DEN is a group of adsorption parameters, α denotes the catalyst activity, k_i and K_i denote the rate and equilibrium constants of reaction i, respectively, P_k and K_K denote the partial pressure and the adsorption constant of component k, respectively (Xu and Froment, 1989b,a).

2.6. Entropy generation rate of reactor

EGR can be used to measure the irreversible losses in the irreversible processes (Kjelstrup and Bedeaux, 2008; Kjelstrup et al., 2010). The local EGR in the MS-SMR reactor is expressed as follows:

$$\sigma_{\mathrm{Tot}} = \sigma_{\mathrm{H,\,MS\text{-}Ro}} + \sigma_{\mathrm{H,\,Ro\text{-}Ri}} + \sigma_{\mathrm{H,\,Ri\text{-}RM}} + \sigma_P + \sum_i \sigma_{r_i} \tag{19}$$

where $\sigma_{\mathrm{H,\,MS\text{-}Ro}}$, $\sigma_{\mathrm{H,\,Ro\text{-}Ri}}$, and $\sigma_{\mathrm{H,\,Ri\text{-}RM}}$ denote the local EGRs attributed to the heat transfer (HT) between the MS and the outer wall of the RT, the outer wall and the inner wall of the RT, the inner tube of RT and the RM, respectively, σ_{r_i} denotes the local EGR attributed to the each reaction, σ_P denotes the local EGR attributed to the viscous flow, and the local EGR of each irreversible process are listed in Table 1.

Table 3
Optimization variables setting of the reference reactor and the value ranges of them.

Optimization variable	Symbol (unit)	Value	Value range
Temperature of the inlet MS	T^0_{MS} (K)	850	[800, 880]
MFR of the inlet MS	F^0_{MS} (mol s^{-1})	32	[20, 50]
Total MFR of the inlet RM	F^0_{T} (mol s^{-1})	6.746	[4, 10]
Steam methane ratio of the inlet RM	S/M	3.3578	[3, 5]
Temperature of the inlet RM	T^0_{RM} (K)	773.15	[700, 850]
Pressure of the inlet RM	P^0_{RM} (bar)	29	[20, 40]

As the optimization objective, the total EGR Sg(L) is expressed as follows:

$$\mathrm{Sg(L)} = \mathrm{Sg_H(L)} + \mathrm{Sg_r(L)} + \mathrm{Sg_P(L)} = \frac{\mathrm{d}S}{\mathrm{d}t} = \int_0^L \sigma_{\mathrm{Tot}} \mathrm{d}z \tag{20}$$

where, $\mathrm{Sg_H(L)}$, $\mathrm{Sg_r(L)}$, and $\mathrm{Sg_P(L)}$ denote the total EGR attributed to the HT, the chemical reaction, and the viscous flow, respectively.

2.7. Model verification

To verify the reliability of the reaction kinetic and some thermodynamic models in Appendix A, the simulation results of an isothermal and isobaric SMR reactor based on the above models are compared with the results under the thermodynamic equilibrium and the experimental (Shu et al., 1994; Gallucci et al., 2004). All parameters in the isothermal and isobaric SMR reactor are obtained from the experimental parameters of Shu et al. (1994). The methane conversion rate versus the temperature of the RM under the simulation, thermodynamic equilibrium and experimental is shown in Fig. 3. As shown in Fig. 3, the methane conversion rate under the thermodynamic equilibrium is higher than that under the simulation and experimental results. The error between the simulation results and the experimental results is slightly larger in the low-temperature section. However, in the range of 675 K to 725 K, the reliability of the above models shows the best, which indicates that the above models can be used to describe the MS-SMR reactor within the research scope.

3. Optimal performance

3.1. Description of optimization problem

The MS-SMR reactor is modified on the basis of the traditional SMR reactor. Therefore, selecting optimization variables and setting the values of all parameters must be based on the following principles (Månsson and Andressen, 1986): (1) the geometric parameters of the traditional SMR reactor should not be changed as far as possible; (2) adjusting the optimization variables should not affect other facilities as much as possible; (3) the ranges of the optimization variables should be obtained from the references or

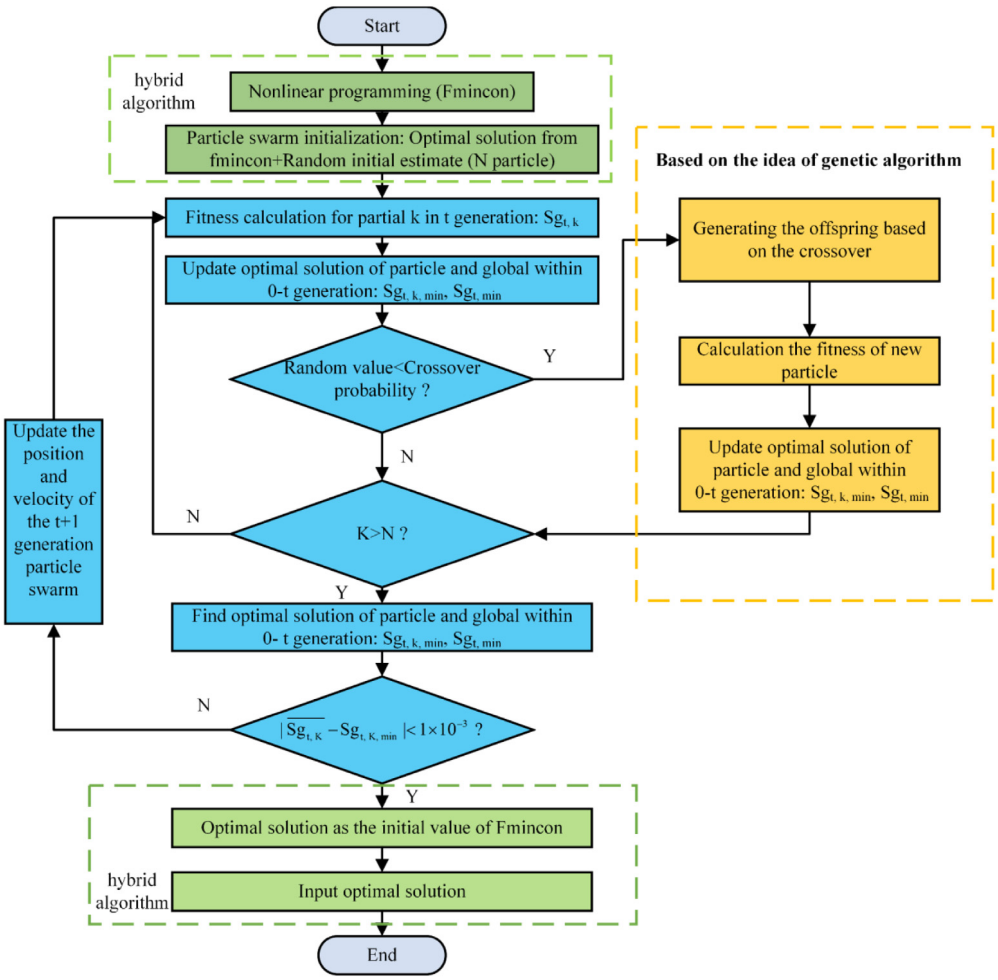

Fig. 4. Hybrid particle swarm optimization algorithm flow chart.

the plant data; (4) other parameters except for the optimization variables are consistent with the traditional SMR reactor. According to the above principles, some inlet operating parameters are chosen as the optimization variables. The fixed HPR, which is obtained by solving the reference reactor model, the conservation equations, and the boundary constraints of the optimization variables are considered as the constraints. The minimum total EGR is chosen as the optimization objective.

3.2. Classification of optimization problems

In the optimization problem, the performance of the optimization objective can be improved by increasing the freedoms (Johannessen and Kjelstrup, 2004; Nummedal et al., 2005; Wilhelmsen et al., 2010; Zhang et al., 2018; Li et al., 2019a; Chen et al., 2018b; Kingston and Razzitte, 2018). According to the number of the optimization variables, the reference reactor and four types of optimal reactors in this paper are obtained as follows:

(1) Reference reactor: all optimization variables are given according to the references or the plant data.

(2) Case 1: the temperature and MFR of the inlet MS are taken as the optimization variables, and other parameters are consistent with the reference reactor.

(3) Case 2: the total MFR and S/M of the inlet RM are added as the optimization variables based on the Case 1 reactor.

(4) Case 3: the temperature of the inlet RM is added as the optimization variables based on the Case 2 reactor.

(5) Case 4: the pressure of the inlet RM is added as the optimization variables based on the Case 3 reactor.

3.3. Numerical computation method

Above optimization problem belongs to a multi-dimension and multi-peak nonlinear optimization problem, solved by using the intelligent optimization algorithms. For the large-scale nonlinear continuous optimization problems, the particle swarm optimization owns the advantages of high efficiency and correctness (Azab, 2020). However, it may be trapped in the local optimal solution sometimes (Qian et al., 2012; Zhou et al., 2014). The genetic algorithm can ensure the population diversity through the crossover and mutation of the genetic operators, so as to obtain the global optimal solution, whereas it generally consumes a lot of computational resources. The computational efficiency and correctness of the non-linear programming are higher than those of other methods in solving the small-scale nonlinear optimization problems. However, the optimal solution obtained by utilizing the non-linear programming is easily trapped in the local optimal solution in solving the multi-dimensional and multi-peak optimization problems. As the increasing optimization variables, the calculation precision of the particle swarm optimization decreases and the calculation time increase. To obtain the global optimal solution within less time, the hybrid particle swarm optimization algorithm as shown in Fig. 4 is proposed. In the optimization process, the swarm size, the crossover probability, the

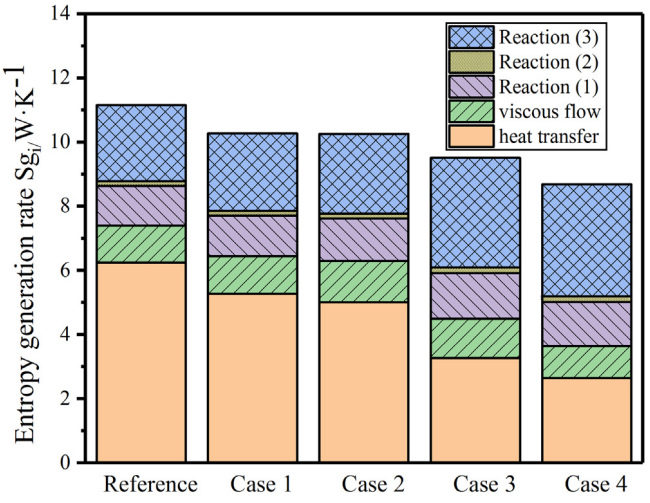

Fig. 5. The comparisons of the EGRs of the irreversible processes in each reactor.

learning factor of the individual optimization, the learning factor of the global optimization, the inertia factor, and the maximum permission iterative number are set as 100, 0.04, 2, 2, 0.8, and 300, respectively.

4. Results and discussions

4.1. Parameters setting of reference reactor

All parameters of the reactor and catalyst are consistent with those parameters in the practical industrial SMR reactor (Xu and Froment, 1989b,a). The catalyst Ni/$MgAl_2O_4$ is not a regular spherical particle. Therefore, the porosity of the CB is set as 0.65, according to the industrial reactors (Johannessen and Kjelstrup, 2004; Zhang et al., 2018, 2020; Li et al., 2019a; Chen et al., 2018b; Wesenberg, 2006). The heat flux between the MS and the RM, and the intraparticle diffusion effective factors of the reference reactor are calculated by using the HT model and the catalyst particle model (Zhang et al., 2019; Hicks, 1970), respectively. The catalyst activity is set as 1. The heat capacities and reaction enthalpies of the RM can be obtained from Ref. Johannessen and Kjelstrup (2004). The viscosities, and thermal conductivities of the RM and MS are calculated based on the empirical formulas as shown in Appendix A (Yaws, 1999). Tables 2 and 3 list the major parameters and the optimization variables of the MS-SMR reactor, respectively.

4.2. Numerical results

The flow direction of the MS is opposite to that of the RM in this paper. Therefore, solving the reference reactor model belongs to a two-point boundary value problem, which generally is solved by using the function of 'bvp4c' in MATLAB. That function is also needed to solve the catalyst particle model (Kingston and Razzitte, 2018), which consists of a set of second-order differential equation. The hybrid particle swarm optimization is used to optimize Case 1- Case 4 reactors. To shorten the calculation time for searching the global optimal solution, the intraparticle diffusion effective factor of each reaction is set as 0.04, 0.1, and 0.04, respectively, according to the calculation results of the reference reactor.

Table 4 lists the optimal values of the optimization variables, the methane conversion rate and the total EGR of each reactor and the corresponding decreased magnitude. As shown in Table 4,

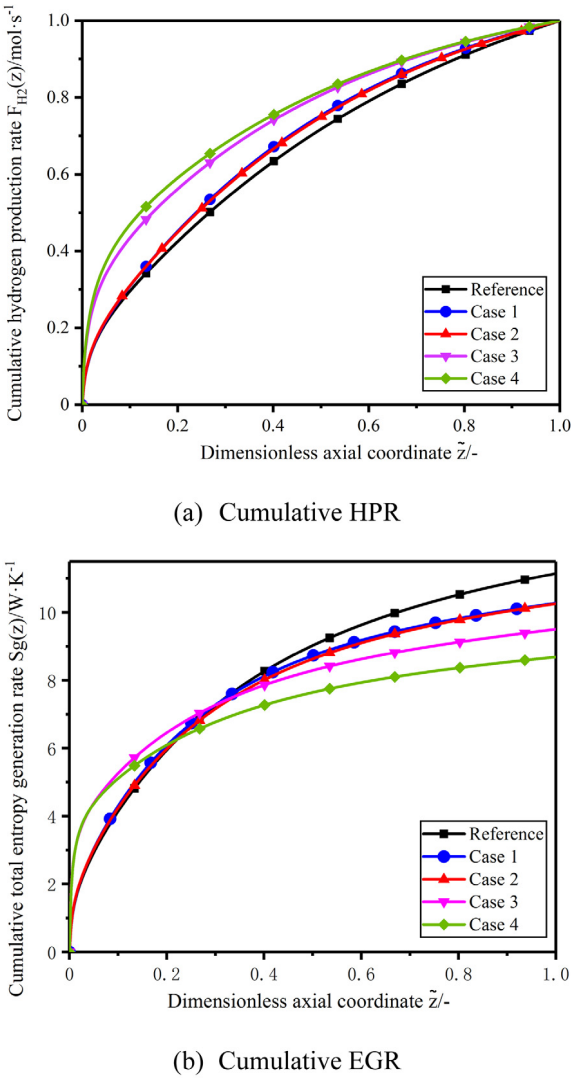

Fig. 6. The distributions of the cumulative HPR and EGR in each reactor.

Table 4
Optimal values of the optimization variables, the methane conversion rate and the total EGR of each reactor and corresponding decreased magnitude.

Reactor	Reference	Case 1	Case 2	Case 3	Case 4
T^0_{MS} (K)	863.35	851.17	846.89	853.75	851.46
F^0_{MS} (mol s^{-1})	32	50	50	50	50
S/M	3.35	3.35	3.06	5	5
F^0_T (mol s^{-1})	6.746	6.746	6.950	6.764	8
T^0_{RM} (K)	773.15	773.15	773.15	823.81	833.60
P^0_{RM} (bar)	29	29	29	29	40
X_{CH_4} (%)	17.8	17.8	16.1	24.5	20.6
Sg(L) (W K^{-1})	11.14	10.27	10.26	9.50	8.68
Decreased magnitude (%)	–	7.81	7.90	14.72	22.08

the total EGRs of the optimal reactors decrease with the increasing number of optimization variables. Compared with the total EGR of the reference reactor, that of the Case 4 reactor decreases by 22.08%. The methane conversion rate of the Case 3 reactor (24.5%) is higher than that of other reactors. That is due to the higher S/M and the lower pressure in the Case 3 reactor, and they are favorable to improve the methane conversion, according to the Le Chatelier's principle. On the basis of the Case 1 reactor, releasing the total MFR and the S/M of the inlet RM has a slight influence on the total EGR of the optimal reactor.

Table 5
The minimum EGRs and the optimal design parameters of the Case 4 reactor with each catalyst activity.

	$\alpha = 0.6$	$\alpha = 0.3$	$\alpha = 0.2$	$\alpha = 0.15$
T^0_{MS} (K)	862	876	880	880
F^0_{MS} (mol s^{-1})	50	50	50	50
S/M	5	3.07	3	3
F^0_T (mol s^{-1})	7.49	6.68	6.93	7.52
T^0_{RM} (K)	850	850	850	850
P^0_{RM} (bar)	40	40	40	40
X_{CH_4} (%)	22.1	16.9	16.01	14.7
Sg(L) (W K^{-1})	8.70	9.09	9.61	10.27

Fig. 5 illustrates the comparisons of the EGRs of the irreversible processes in each reactor. As shown in Fig. 5, some optimization variables have different effects on the EGRs from different irreversible processes. For example, optimizing the total MFR and the S/M of the inlet RM decreases the EGR attributed to the HT, while it increases the EGRs attributed to the chemical reactions and the viscous flow processes. Therefore, the total EGR of the Case 2 reactor is basically consistent with that of the Case 1 reactor. Optimizing the temperature of the inlet RM decreases the EGR attributed to the HT, meanwhile, it significantly increases the EGR attributed to the reaction (3). The EGRs from the HT and the viscous flow are reduced by optimizing the pressure of the inlet RM. From the perspective of decision makers, one can find out the impact of each operating parameter on the EGR of each irreversible process, and then adjusts some key operating parameter to reduce the total EGR.

Fig. 6 illustrates the profiles of the cumulative HPR and total EGR in each reactor. As shown in Fig. 6(a), the profiles of the cumulative HPRs show a sharp increase, and then are followed by a slight increase up to the value of 1 mol/s. That is due to the decreasing reactants along the axial of reactor. As shown in Fig. 6(b), the profiles of the cumulative total EGRs in the reference reactor and the Case 1 and Case 2 reactors are basically the same near the inlet, while these profiles are slightly different near the outlet. This is because that the local EGR due to the heat transfer is much less than that due to the chemical reaction at the inlet of reactor, and optimizing the temperature and the MFR of the molten salt has a little influence on the local EGR due to the chemical reactions. The cumulative total EGRs of the Case 3 and Case 4 reactors are larger than that of other reactors near the inlet. This is because that increasing the temperature and the pressure of the RM results in the increasing reaction rates at the inlet, and then causes the increasing local EGRs due to the chemical reactions. However, the total EGRs of the Case 3 and Case 4 reactors are smaller than that of other reactors at the outlet. That is because that the EGR due to the heat transfer decreases with the increase of the temperature of the RM. According to Figs. 5 and 6, the irreversibility of the reference reactor and the Case 1 and Case 2 reactors mainly comes from the HT processes, while that of the Case 3 and Case 4 reactors mainly comes from the chemical reaction processes.

Fig. 7 illustrates the profiles of the temperatures of the RM and the MS in each reactor. The temperature profiles show a decrease up to the minimum near the inlet, and then are followed by a linear increase. This is because that the heat required for the endothermic reactions at the inlet is much greater than the heat adsorbed of the reaction mixture from the molten salt, and the reaction rates decrease along the axial of the reactor, which leads to a significant reduction in the heat required for the endothermic reactions. The temperature of the inlet MS in the Case 1 reactor is much less than that in the reference reactor, that is due to the increasing MFR of the inlet MS. The temperature differences

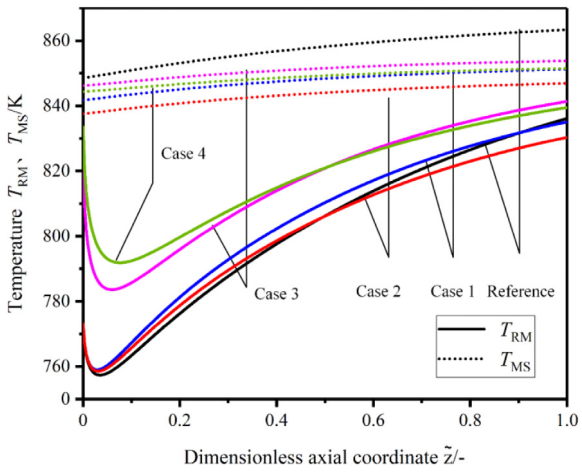

Fig. 7. The distributions of the temperatures of the RM and the MS in each reactor.

between the MS and the RM in the Case 3 and Case 4 reactors are much less than that in other reactors, that is due to the increasing temperature of the RM and the decreasing temperature of the inlet MS.

Fig. 8 illustrates the profiles of the driving force and local EGR of the HT process in each reactor. As shown in Fig. 8(a), the profiles of the thermal forces show a sharp increase up to a maximum, and then are followed by an approximately linear decrease, and these profiles are similar to that of the temperature differences. The profile of the thermal force of each reactor gradually decreases, and distributes more even along the dimensionless axial coordinate with the increasing number of the optimization variables. This phenomenon can be explained by using the equipartition principles of the driving force (Sauar et al., 1996). As shown in Fig. 8(b), the profiles of the local EGRs attributed to the HT are basically similar to that of the thermal forces in all reactors except for the Case 1 reactor. The Case 1 reactor owns the maximum local EGR attributed to the HT, while its thermal force is not the maximum. That is because that increasing the MFR of the inlet MS leads to the increase of the HT coefficient between the MS and the RM, and then causing the increasing heat flux and local EGR. The optimal results shown in Fig. 8 verify the equipartition principles of driving force and entropy generation (Sauar et al., 1996; Tondeur and Kvaalen, 1987).

Fig. 9 illustrates the profiles of the cumulative and local EGRs attributed to the chemical reactions in each reactor. As shown in Fig. 9(a), about 85% of the EGR distributes in the first 10% length of each reactor, that is due to the sufficient reactants near the inlet of each reactor. The total EGR attributed to the chemical reaction in each reactor increases with the increasing number of optimization variables. As shown in Fig. 9(b), the local EGR attributed to the chemical reaction is larger than that attributed to the HT and viscous flow processes at the inlet of each reactor. Therefore, the profile of the cumulative EGR attributed to the chemical reaction is similar to that of the cumulative total EGR at the inlet of each reactor. The local EGRs attributed to the chemical reactions near the inlet of the Case 3 and Case 4 reactors are larger than that of other reactors, that is due to the increasing temperature and pressure of the inlet RM. According to Figs. 5 and 9(b), for the chemical reactions processes in each reactor, the more uneven the profile of the local EGR is, the larger the total EGR is. This phenomenon verifies the principle of equipartition entropy generation (Tondeur and Kvaalen, 1987).

Fig. 10 illustrates the profiles of the driving force and the local EGR of the viscous flow process in each reactor. As shown in

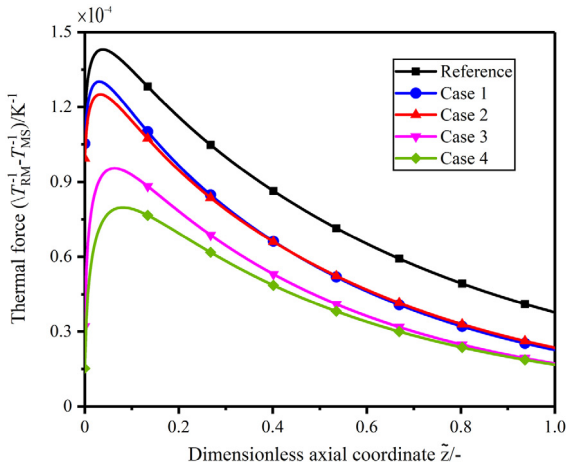

(a) Thermal force

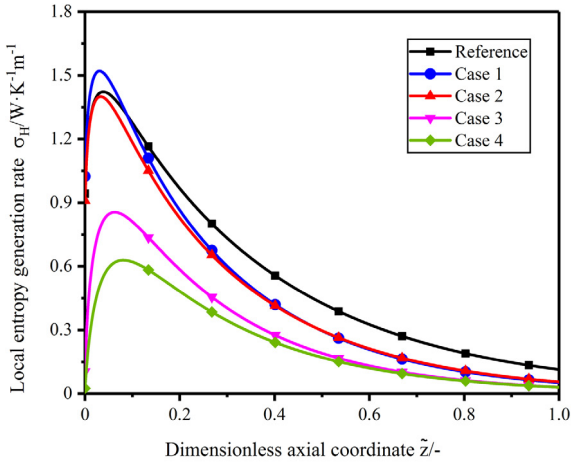

(b) Local EGR attributed to the HT

Fig. 8. The distributions of the driving force and local EGR of the HT process in each reactor.

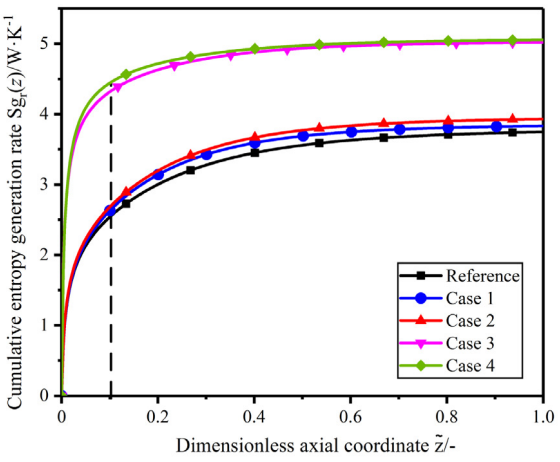

(a) Cumulative EGR attributed to the chemical reactions

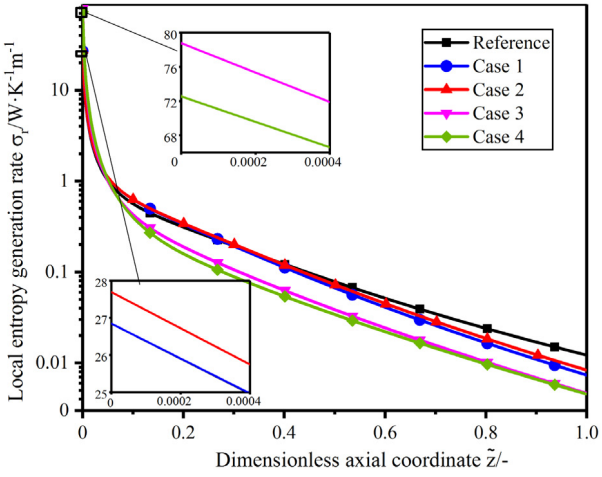

(b) Local EGR attributed to the chemical reactions

Fig. 9. The distributions of the cumulative and local EGRs attributed to the chemical reactions in each reactor.

Fig. 10(a), the profile of the driving force of the viscous flow process in each reactor shows a sharp decrease, and then is followed by a slight decrease. This phenomenon is because that the total MFR and the velocity of the RM increase rapidly due to the largest reaction rates near the inlet of each reactor, and then they increase slightly due to the decreasing reaction rates and the increasing temperature of the inlet RM. As shown in Fig. 10(b), the local EGRs in the Case 2 and Case 3 reactors are larger than that in other reactors, that is due to the increasing total MFR of the inlet RM. The Case 4 reactor owns the minimum local EGR because of the largest pressure of the inlet RM.

The porosity of CB is utilized to characterize the structure of the CB. The ideal porosity of the CB is generally above 0.375 (Pushnov, 2006), and the porosity of the CB in the industrial reactors is generally above 0.5 (Wesenberg, 2006). The porosity of the CB studied in this paper is considered to vary from 0.375 to 0.65. Fig. 11 illustrates the influence of the porosity of the CB on the total EGR and the optimal value of each optimization variable. Regardless of the value of the porosity of the CB, the optimal MFR of the inlet MS and the optimal pressure of the inlet RM are equal to 50 mol/s and 40 bar, respectively, hence the profiles of them are not shown in Fig. 11. As shown in Fig. 11, within the scope of the porosity of the CB, the profiles of the total EGR show a sharp decrease, and then are followed by a slight decrease. The reasons for the above phenomenon mainly include two reasons: (1) increasing the porosity of the CB leads to the decreasing flow resistance and the total EGR attributed to the viscous flow; (2) the local EGRs attributed to the HT show a sharp decrease, and then are followed by a decrease with the increasing porosity of the CB. Increasing the porosity of the CB leads to the decreasing contact area between the RM and the catalyst surface, and hence the total MFR and the S/M of the inlet RM must be increased to meet the constraint of the fixed HPR.

The deactivation of the catalyst is inevitable in the practical chemical reaction process. Fig. 12 illustrates the HPR versus the catalyst activity under the optimal parameters of the Case 4 reactor. As shown in Fig. 12, the profile of HPR shows a slight decrease, and then are followed by a sharp decrease. To ensure the fixed HPR, the optimization variables of the reactor should be adjusted according to the real-time optimization (Paulen and Fikar, 2019). However, it is suitable for the small-scale optimization problem, which does not need consume a lot of computational time. For this large-scale optimization problem, calculating optimal operating parameters in advance for different catalyst activity, and then invoking the operating parameters corresponding to the catalyst activity is better.

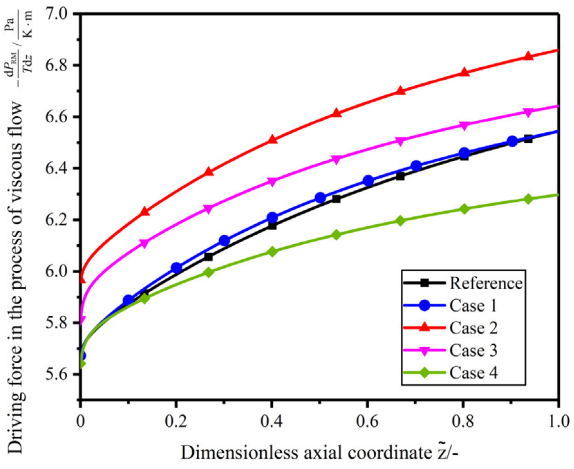

(a) Driving force attributed to the viscous flow

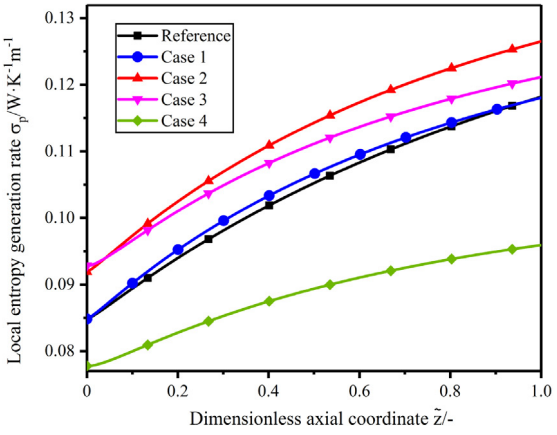

(b) Local EGR attributed to the viscous flow

Fig. 10. The distributions of the driving force and the local EGR of the viscous flow process in each reactor.

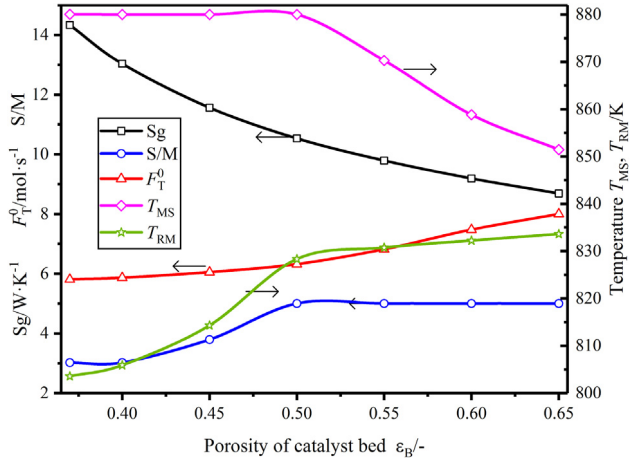

Fig. 11. The total EGR and the optimal value of each optimization variable versus the porosity of the CB.

Table 5 lists the minimum EGRs and the optimal design parameters of the reactors with the catalyst activity being 0.6, 0.3, 0.2 and 0.15, respectively. As shown in Table 5, with the

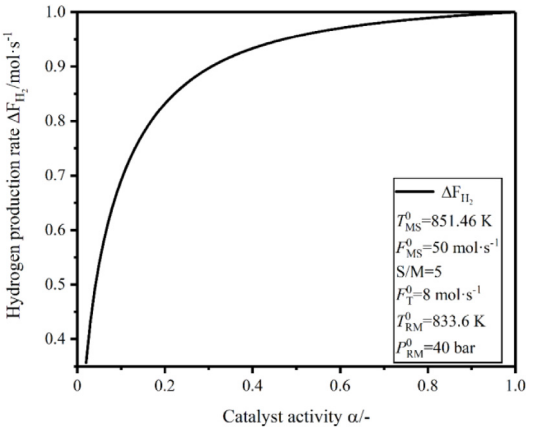

Fig. 12. The HPR versus the catalyst activity under the optimal parameters of the Case 4 reactor.

decreasing catalyst activity in the scope of the study, the fixed HPR can still be obtained by adjusting the optimization variables. Decreasing the catalyst activity leads to the increasing optimal inlet temperature of the MS and the RM, meanwhile, it leads to the decreases of the optimal total MFR and the S/M of the inlet RM. The methane conversion rate decreases with the decreasing catalyst activity. Le Chatelier principle indicates that increasing the MFR of the inlet methane, and the temperature of the inlet RM and the MS are conductive to produce hydrogen. Therefore, the S/Ms and the temperatures of the inlet RM, and the temperatures of the inlet MS reach the maximums, when the catalyst activities are equal to 0.2 and 0.15. The total EGR is always on the rise and increases much bigger with the decreasing catalyst activity. Therefore, it is inferred that as the catalyst activity is further reduced, adjusting the operating parameters cannot compensate for the decreasing HPR attributed to the decreasing catalyst activity.

5. Conclusion

This paper performs the performance optimization of the MS-SMR reactor by using finite-time thermodynamics and the hybrid particle swarm optimization, where the minimum total EGR and the fixed HPR are chosen as the optimization objective and the constraints, respectively. The effects of the porosity of the CB and the catalyst activity on the thermodynamic optimization results are analyzed. Some important conclusions are as follows:

(1) The total EGR of the MS-SMR reactor is reduced by 22.08% after optimizing the inlet parameters of the molten salt and reaction mixture.
(2) With the increasing number of optimization variables in each reactor, the total EGR, and the EGR attributed to the HT continuously decrease, while the EGR attributed to the chemical reaction continuously increases. The total EGR of the MS-SMR reactor is reduced by 22.08% by optimizing the inlet parameters of the molten salt and reaction mixture.
(3) The equipartition principles of entropy generation and driving force are verified by the profiles of the local EGR and driving force in each irreversible process.
(4) Within the scope of the study, increasing the porosity of the CB leads to the increasing total EGR of the optimal reactor.
(5) Within the scope of the study, adjusting the operating parameters of the reactor can cope with the decreasing HPR attributed to the decreasing catalyst activity. However, the decreasing catalyst activity leads to the increasing total EGR, and the decreasing methane conversion rate.

The obtained results are favorable to guide the optimal design of the practical reactors, and to optimize overall process for hydrogen production including the MS-SMR reactor in the future work.

Declaration of competing interest

The authors declare that they have no known competing financial interests or personal relationships that could have appeared to influence the work reported in this paper.

CRediT authorship contribution statement

Penglei Li: Methodology, Software, Validation, Data curation, Writing - original draft. **Lingen Chen:** Funding acquisition, Conceptualization, Supervision, Writing - review & editing. **Shaojun Xia:** Funding acquisition, Methodology, Software, Validation, Writing - original draft. **Lei Zhang:** Software, Validation. **Rui Kong:** Software, Validation. **Yanlin Ge:** Software, Validation. **Huijun Feng:** Software, Validation.

Acknowledgment

This paper is supported by the National Natural Science Foundation of PR China (Grant Nos. 51976235 and 51606218) and the Hubei Province Natural Science Foundation of China (Grant No, 2018CFB708), Self-Topic Project of Naval University of Engineering (Project No. 20161504). The authors wish to thank the reviewers for their careful, unbiased and constructive suggestions, which led to this revised manuscript.

Appendix A

The molar heat capacity at a constant pressure of each component is expressed as follows (Yaws, 1999)

$$C_{P,\,CH_4} = 34.942 - 3.9957\times10^{-2}\cdot T + 1.9184\times10^{-4}\cdot T^2 - 1.5303\times10^{-7}\cdot T^3 + 3.9321\times10^{-11}\cdot T^4 \quad (A.1)$$

$$C_{P,\,H_2O} = 33.933 - 8.4186\times10^{-3}\cdot T + 2.9906\times10^{-5}\cdot T^2 - 1.78250\times10^{-8}\cdot T^3 + 3.6934\times10^{-12}\cdot T^4 \quad (A.2)$$

$$C_{P,\,H_2} = 25.399 + 2.0178\times10^{-2}\cdot T - 3.8549\times10^{-5}\cdot T^2 + 3.188\times10^{-8}\cdot T^3 - 8.7585\times10^{-12}\cdot T^4 \quad (A.3)$$

$$C_{P,\,CO} = 29.556 - 6.5807\times10^{-3}\cdot T + 2.0130\times10^{-5}\cdot T^2 + 3.9968\times10^{-9}\cdot T^3 - 2.9872\times10^{-13}\cdot T^4 \quad (A.4)$$

$$C_{P,\,CO_2} = 27.437 + 4.2315\times10^{-2}\cdot T - 1.9555\times10^{-5}\cdot T^2 - 1.2227\times10^{-8}\cdot T^3 + 2.2617\times10^{-12}\cdot T^4 \quad (A.5)$$

$$C_{P,\,N_2} = 29.342 - 3.5395\times10^{-3}\cdot T + 1.0076\times10^{-5}\cdot T^2 - 4.3116\times10^{-9}\cdot T^3 + 2.5935\times10^{-13}\cdot T^4 \quad (A.6)$$

The reaction enthalpy of each reaction is expresses as follows (Poling et al., 2001)

$$\Delta_r H_{T,i} = \sum_k \left(\upsilon_{k,i}\Delta_f H_{T,k}\right) \quad (A.7)$$

$$\Delta_f H_{T,k} = \int C_{p,\,k}\mathrm{d}T \quad (A.8)$$

where $\upsilon_{k,i}$ and $\Delta_f H_{T,k}$ are the stoichiometric number and the molar formation enthalpy, respectively.

The viscosity of each component is expressed as follows (Yaws, 1999)

$$\mu_{CH_4} = 3.844 + 4.011\times10^{-1}\cdot T - 1.130\times10^{-4}\cdot T^2 \quad (A.9)$$

$$\mu_{H_2O} = -36.826 + 4.2900\times10^{-1}\cdot T - 1.6200\times10^{-5}\cdot T^2 \quad (A.10)$$

$$\mu_{H_2} = 27.758 + 2.1200\times10^{-1}\cdot T - 3.2800\times10^{-5}\cdot T^2 \quad (A.11)$$

$$\mu_{CO} = 23.811 + 5.3944\times10^{-1}\cdot T - 1.5411\times10^{-4}\cdot T^2 \quad (A.12)$$

$$\mu_{CO_2} = 11.811 + 4.980\times10^{-1}\cdot T - 1.090\times10^{-4}\cdot T^2 \quad (A.13)$$

$$\mu_{N_2} = 42.606 + 4.7500\times10^{-1}\cdot T - 9.8800\times10^{-5}\cdot T^2 \quad (A.14)$$

The thermal conductivity of each component is expressed as follows (Yaws, 1999)

$$\lambda_{CH_4} = -0.0094 + 1.4030\times10^{-4}\cdot T + 3.3180\times10^{-7}\cdot T^2 \quad (A.15)$$

$$\lambda_{H_2O} = 0.00053 + 4.7093\times10^{-5}\cdot T + 4.9551\times10^{-8}\cdot T^2 \quad (A.16)$$

$$\lambda_{H_2} = 0.03951 + 4.5918\times10^{-4}\cdot T - 6.4933\times10^{-8}\cdot T^2 \quad (A.17)$$

$$\lambda_{CO} = 0.00158 + 8.2511\times10^{-5}\cdot T - 1.9081\times10^{-8}\cdot T^2 \quad (A.18)$$

$$\lambda_{co_2} = -0.012 + 1.0208\times10^{-4}\cdot T - 2.2403\times10^{-8}\cdot T^2 \quad (A.19)$$

$$\lambda_{N_2} = 0.00309 + 7.5930\times10^{-5}\cdot T - 1.1014\times10^{-8}\cdot T^2 \quad (A.20)$$

The thermal conductivity of reaction mixture is derived from Refs. Wesenberg (2006) and Falco et al. (2007):

$$\lambda_{RM} = \sum_{k=1}^{6}\frac{x_k\lambda_k}{\sum_{j=1}^{6}x_jA_{k,j}} \quad (A.21)$$

$$A_{k,j} = 0.25\left\{1+\left[\frac{\mu_k}{\mu_j}\left(\frac{M_j}{M_k}\right)^{3/4}\frac{T+\vec{S}_k}{T+\vec{S}_j}\right]^{1/2}\right\}^2\frac{T+\vec{S}_{k,j}}{T+\vec{S}_j} \quad (A.22)$$

where $\vec{S}_k = 1.5\cdot T_{b,k}$, $\vec{S}_{k,k} = \vec{S}_k$, $\vec{S}_{k,j} = \vec{S}_{j,k}$, $\vec{S}_{k,j} = 0.735\sqrt{\vec{S}_k\cdot\vec{S}_j}$, $T_{b,k}$ is the boiling temperature of gas except for hydrogen under standard atmosphere pressure, and $T_{b,H_2} = 79$ K.

The viscosity of the MS is written as follows (Zavoico, 2001)

$$\mu_{MS} = \left[22.7 - 0.12\,(T_{MS}-273) + 2.2\times10^{-4}\,(T_{MS}-273)^2 - 1.4\times10^{-7}\,(T_{MS}-273)^3\right]\times10^{-3} \quad (A.23)$$

The molar heat capacity of the MS is written as follows (Zavoico, 2001)

$$C_{P,MS} = 127.6508 + 1.57\times10^{-2}\cdot T_{MS} \quad (A.24)$$

The thermal conductivity of the MS is written as follows (Zavoico, 2001)

$$\lambda_{MS} = 0.391 + 1.9\times10^{-4}\times T_{MS} \quad (A.25)$$

Appendix B

The convective HT coefficient h_{MS}^{Ro} is written as follows (Gnielinski, 2009)

$$h_{MS}^{Ro} = \frac{(f/8)\,(Re_{MS}-1000)\,Pr_{MS}^{T_{MS}}}{1+12.7\sqrt{f/8}\left(Pr_{MS}^{T_{MS}\,2/3}-1\right)}\left[1+\left(\frac{D_H}{L}\right)^{2/3}\right]\times\left(\frac{Pr_{MS}^{T_{MS}}}{Pr_{MS}^{T_{Ro}}}\right)^{0.01}F\frac{\lambda_{MS}}{D_H} \quad (B.1)$$

$$f = (1.82 \lg Re_{MS} - 1.64)^{-2} \tag{B.2}$$

$$F = 0.86(d_{Hi}/d_{Ro})^{-0.16} \tag{B.3}$$

where f denotes the Darcy resistance coefficient under turbulent, F denotes a modified coefficient to the annular heating tube model, d_{Hi} and D_H denote the inner and hydraulic diameter of the annular heating tube, respectively, Re_{MS} denotes the Reynolds number for the annular tube, and $Pr_{MS}^{T_{MS}}$ and $Pr_{MS}^{T_{Ro}}$ denote the Prandtl numbers representing the relative importance between the momentum exchange and the heat exchange under T_{MS} and T_{Ro} in annular tube, respectively.

The overall HT coefficient for RT h_{RT} is written as follows (Falco et al., 2007)

$$h_{RT} = \left[\frac{1}{h_{Ri}^{RM}} + \frac{1}{6}\cdot\frac{d_{Ro}}{\lambda_B}\cdot\frac{Bi+3}{Bi+4}\right]^{-1} \tag{B.4}$$

where $Bi = \left(h_{Ri}^{RM}\cdot d_{Ro}\right)/(2\lambda_C)$ denotes the Biot number, h_{Ri}^{RM} denotes the convective HT coefficient between the RM and the inner wall of RT, λ_B is the effective radial thermal conductivity (De Wasch and Froment, 1972).

$$\lambda_B = \lambda_B^0 + 0.111\cdot\lambda_{RM}\cdot\frac{Re_C\cdot Pr_{RM}^{1/3}}{1+46\,(d_C/d_{Ri})} \tag{B.5}$$

The radial thermal conductivity in the absence of fluid flow in the CB λ_B^0 is expressed as follows (Kunii and Smith, 1960)

$$\lambda_B^0 = \varepsilon_B\,(\lambda_{RM} + 0.95\cdot\sigma_{ru}\cdot d_C) + \frac{0.95\,(1-\varepsilon_B)}{2/(3\lambda_C) + 1/(10\lambda_{RM}+\sigma_{rs}\cdot d_C)} \tag{B.6}$$

where σ_{ru} and σ_{rs} denote the radiant HT coefficients between the RM and the catalyst particles, and between the catalyst particles and the catalyst particles (Yagi and Kunii, 1957).

The surface HT coefficient between the catalyst particles and the RM is expressed as follows (Yagi and Wakao, 1959):

$$h_{Ri}^{RM} = 0.2\cdot G_{RM}\cdot c_{p,m}\cdot Re_C^{-0.2}\cdot Pr_{RM}^{-2/3}$$
$$\text{s.t. } 0.05 < d_C/d_{Ri} < 0.3 Re_C > 20 \tag{B.7}$$

References

Abam, F.I., Ekwe, E.B., Effiom, S.O., Ndukwu, M.C., 2018. A comparative performance analysis and thermo-sustainability indicators of modified low-heat organic rankine cycles (ORCs) an exergy-based procedure. Energy Rep. 4, 110–118.

Açıkkalp, E., Chen, L.G., Ahmadi, M.H., 2020. Comparative performance analyses of molten carbonate fuel cell-alkali metal thermal to electric converter and molten carbonate fuel cell-thermoelectric generator hybrid systems. Energy Rep. 6, 10–16.

Albassam, A., Conner, J., Manousiouthakis, V., 2018. Natural gas derived hydrogen in the presence of carbon fuel taxes and concentrated solar power. Acs. Sustain. Chem. Eng. 6 (3), 3029–3038.

Alotaibi, S., Alotaibi, F., Ibrahim, O.M., 2020. Solar-assisted steam power plant retrofitted with regenerative system using Parabolic Trough Solar Collectors. Energy Rep. 6, 124–133.

Andresen, B., 2011. Current trends in finite-time thermodynamics. Angew. Chem. Int. Edn 50 (12), 2690–2704.

Andresen, B., Berry, R.S., Ondrechen, M.J., Salamon, P., 1984. Thermodynamics for processes in finite time. Acc. Chem. Res. 17 (8), 266–271.

Ao, C.Y., Xia, S.J., Song, H.J., Chen, L.G., 2018. Entropy generation minimization of steam methane reforming reactor with linear phenomenological heat transfer law. Sci. Sin. Tech. 48 (1), 25–38, (in Chinese).

Azab, M., 2020. Multi-objective design approach of passive filters for single-phase distributed energy grid integration systems using particle swarm optimization. Energy Rep. 6, 157–172.

Bejan, A., 1982. Entropy Generation Through Heat and Fluid Flow. Wiley, New York.

Bejan, A., 1996a. Entropy Generation Minimization. CRC Press, Boca Raton FL.

Bejan, A., 1996b. Entropy generation minimization: The new thermodynamics of finite-size devices and finite-time processes. J. Appl. Phys. 79 (3), 1191–1218.

Bejan, A., 1996c. Notes on the history of the method of entropy generation minimization (finite time thermodynamics). J. Non-Equilibrum Thermodyn. 21 (3), 239–242.

Bejan, A., 2013. Enropy generation minimization, exergy analysis, and the constructal law. Arab. J. Sci. Eng. 38 (2), 329–340.

Blooma, R., Hondowa, N., Duponta, V., et al., 2018. Fibrous aluminosilicate catalyst support for hydrogen production by chemical looping steam reforming. Energy Rep. 4, 733–743.

Boyano, A., Blanco-Marigorta, A.M., Morosuk, T., Tsatsaronis, G., 2011. Exergoenvironmental analysis of a steam methane reforming process for hydrogen production. Energy 36 (4), 2202–2214.

Boyano, A., Morosuk, T., Blanco-Marigorta, A.M., Tsatsaronis, G., 2012. Conventional and advanced exergoenvironmental analysis of a steam methane reforming reactor for hydrogen production. J. Clean Prod. 20 (1), 152–160.

Chaubey, R., Sahu, S., James, O.O., Maity, S., 2013. A review on development of industrial processes and emerging techniques for production of hydrogen from renewable and sustainable sources. Renew. Sustain. Energy Rev. 23, 443–462.

Chen, L.G., 2005. Finite-Time Thermodynamic Analysis of Irreversible Processes and Cycles. Higher Education Press, Beijing, (in Chinese).

Chen, B., Liao, Z.W., Wang, J.D., Yu, H.J., Yang, Y.R., 2012. Exergy analysis and CO_2 emission evaluation for steam methane reforming. Int. J. Hydrog. Energy 37 (4), 3191–3200.

Chen, L.G., Sun, F.R., 2004. Advances in Finite Time Thermodynamics: Analysis and Optimization. Nova Science Publishers, New York.

Chen, L.G., Wu, C., Sun, F.R., 1999. Finite time thermodynamic optimization or entropy generation minimization of energy systems. J. Non-Equilibrum Thermodyn. 24 (4), 327–359.

Chen, L.G., Xia, S.J., 2017. Generalized Thermodynamic Dynamic-Optimization for Irreversible Processes. Science Press, Beijing, (in Chinese).

Chen, L.G., Xia, S.J., 2018a. Generalized Thermodynamic Dynamic-Optimization for Irreversible Cycles – Thermodynamic and Chemical Theoretical Cycles. Science Press, Beijing, (in Chinese).

Chen, L.G., Xia, S.J., 2018b. Generalized Thermodynamic Dynamic-Optimization for Irreversible Cycles – Engineering Thermodynamic Plants and Generalized Engine Cycles. Science Press, Beijing, (in Chinese).

Chen, L.G., Xia, S.J., 2019. Progresses in generalized thermodynamic dynamic-optimization of irreversible processes. Sci. Sin. Tech. 49 (9), 981–1022, (in Chinese).

Chen, L.G., Xia, S.J., Feng, H.J., 2019. Progress in generalized thermodynamic dynamic-optimization of irreversible cycles. Sci. Sin. Tech. 49 (11), 1223–1267, (in Chinese).

Chen, Q.X., Xia, S.J., Wang, W.H., Chen, L.G., 2018a. Entropy generation rate minimization of steam methane reforming reactor with Dulong-Petit heat transfer law. Energy Conserv. 37 (3), 31–40, (in Chinese).

Chen, L.G., Zhang, L., Xia, S.J., Sun, F.R., 2018b. Entropy generation minimization for CO_2 hydrogenation to light olefins. Energy 147, 187–196.

De Wasch, A.P., Froment, G.F., 1972. Heat transfer in packed beds. Chem. Eng. Sci. 27 (3), 567–576.

Diglio, G., Hanak, D.P., Bareschino, P., Mancusi, E., Pepe, F., Montagnaro, F., Manovic, V., 2017. Techno-economic analysis of sorption-enhanced steam methane reforming in a fixed bed reactor network integrated with fuel cell. J. Power Sources 364, 41–51.

Falco, M.D., Caputo, G., Frattari, S., Gironi, F., Annesini, M.C., 2014a. Solar steam reforming for enriched methane production: Reactor configurations modeling and comparison. Int. J. Hydrog. Energy 39 (26), 13979–13990.

Falco, M.D., Paola, L.D., Marrelli, L., 2007. Heat transfer and hydrogen permeability in modelling industrial membrane reactors for methane steam reforming. Int. J. Hydrogen Energy 32 (14), 2902–2913.

Falco, M.D., Piemonte, V., Paola, L.D., Basile, A., 2014b. Methane membrane steam reforming: Heat duty assessment. Int. J. Hydrog. Energy 39 (9), 4761–4770.

Feng, H.J., Tao, G.S., Tang, C.Q., Ge, Y.L., Chen, L.G., Xia, S.J., 2019. Exergoeconomic performance optimization for a regenerative gas turbine closed-cycle heat and power cogeneration plant. Energy Rep. 5, 1525–1531.

Gallucci, F., Paturzo, L., Famà, A., Basile, A., 2004. Experimental study of the methane steam reforming reaction in a dense Pd/Ag membrane reactor. Ind. Eng. Chem. Res. 43 (4), 928–933.

Ge, Y.L., Chen, L.G., Sun, F.R., 2016. Progress in finite time thermodynamic studies for internal combustion engine cycles. Entropy 18 (4), 139.

Giaconia, A., Falco, M.D., Caputo, G., Grena, R., Tarquini, P., Marrelli, L., 2008. Solar steam reforming of natural gas for hydrogen production using molten salt heat carriers. AIChE J. 54 (7), 1932–1944.

Gnielinski, V., 2009. Heat transfer coefficients for turbulent flow in concentric annular ducts. Heat Transf. Eng. 30 (6), 431–436.

Guo, F.B., Jia, W.L., Hou, B., et al., 2016. Dry reforming of methane to synthesis gas over lignite semicokes catalyst at high pressure. Energy Rep. 2, 163–170.

Hajjaji, N., Pons, M., Houas, A., Renaudin, V., 2012. Exergy analysis: An efficient tool for understanding and improving hydrogen production via the steam methane reforming process. Energy Policy 42, 392–399.

Hicks, R.E., 1970. Pressure drop in packed beds of spheres. Ind. Eng. Chem. Fundam. 9 (3), 500–502.
Hoseinzade, L., Adams, T.A., 2017. Modeling and simulation of an integrated steam reforming and nuclear heat system. Int. J. Hydrog. Energy 42 (39), 25048–25062.
Jin, J., Wei, X., Liu, M.K., Yu, Y.H., Li, W.J., Kong, H., Hao, Y., 2018. A solar methane reforming reactor design with enhanced efficiency. Appl. Energy 226, 797–807.
Johannessen, E., Kjelstrup, S., 2004. Minimimum entropy production rate in plug flow reactors: An optimal control problem solved for SO_2 oxidation. Energy 29 (12–15), 2403–2423.
Kingston, D., Razzitte, A.C., 2017. Entropy production in chemical reactors. J. Non-Equilib. Thermodyn. 42 (3), 265–276.
Kingston, D., Razzitte, A.C., 2018. Entropy generation minimization in dimethyl ether synthesis: A case study. J. Non-Equilib. Thermodyn. 43 (2), 111–120.
Kjelstrup, S., Bedeaux, D., 2008. Non-Equilibrium Thermodynamics of Heterogeneous Systems. World Scientific, Singapore.
Kjelstrup, S., Bedeaux, D., Johannessen, E., Gross, J., 2010. Non-Equilibrium Thermodynamics for Engineers. World Scientific, Singapore.
Kjelstrup, S., Johannessen, E., Røsjorde, A., Nummedal, L., Bedeaux, D., 2000. Minimizing the entropy production of the methanol producing reaction in a methanol reactor. Int. J. Thermodyn. 3 (4), 147–153.
Kunii, D., Smith, J.M., 1960. Heat transfer characteristics of porous rocks. AIChE J. 6 (1), 71–78.
Leites, I.L., Sama, D.A., Lior, N., 2003. The theory and practice of energy saving in the chemical industry: some methods for reducing thermodynamic irreversibility in chemical technology processes. Energy 28 (1), 55–97.
Li, P.L., Chen, L.G., Xia, S.J., Zhang, L., 2019a. Entropy generation rate minimization for methanol synthesis via a CO_2 hydrogenation reactor. Entropy 21 (2), 174.
Li, P.L., Chen, L.G., Xia, S.J., Zhang, L., 2019b. Maximum hydrogen production rate optimization for tubular steam methane reforming reactor. Int. J. Chem. React. Eng. 17 (9), 20180191.
Lucia, U., Grisolia, G., 2019. Exergy inefficiency: An indicator for sustainable development analysis. Energy Rep. 5, 62–69.
Månsson, B., Andressen, B., 1986. Optimal temperature profile for an ammonia reactor. Ind. Eng. Chem. Process Des. Dev. 25 (1), 59–65.
Nummedal, L., Kjelstrup, S., Costea, M., 2003. Minimizing the entropy production rate of an exothermic reactor with a constant heat-transfer coefficient: the ammonia reaction. Ind. Eng. Chem. Res. 42 (5), 1044–1056.
Nummedal, L., Røsjorde, A., Johannessen, E., Kjelstrup, S., 2005. Second law optimization of a tubular steam reformer. Chem. Eng. Process. 44 (4), 429–440.
Pantoleontos, G., Kikkinides, E.S., Georgiadis, M.C., 2012. A heterogeneous dynamic model for the simulation and optimisation of the steam methane reforming reactor. Int. J. Hydrogen Energy 37 (21), 16346–16358.
Pashchenko, D., 2018. Effect of the geometric dimensionality of computational domain on the results of CFD-modeling of steam methane reforming. Int. J. Hydrogen Energy 43 (18), 8662–8673.
Pashchenko, D., 2019a. Experimental investigation of reforming and flow characteristics of a steam methane reformer filled with nickel catalyst of various shapes. Energy Convers. Manage. 185, 465–472.
Pashchenko, D., 2019b. Experimental investigation of synthesis gas production by methane reforming with flue gas over a NiO-Al_2O_3 catalyst: Reforming characteristics and pressure drop. Int. J. Hydrog. Energy 44 (14), 7073–7082.
Pashchenko, D., 2019c. Experimental study of methane reforming with products of complete methane combustion in a reformer filled with a nickel-based catalyst. Energy Convers. Manage. 183, 159–166.
Paulen, R., Fikar, M., 2019. Dynamic real-time optimization of batch processes using Pontryagin's minimum principle and set-membership adaptation. Comput. Chem. Eng. 128, 488–495.
Piña, J., Schbib, N.S., Bucalá, V., Borio, D.O., 2001. Influence of the heat-flux profiles on the operation of primary steam reformers. Ind. Eng. Chem. Res. 40 (23), 5215–5221.
Piemonte, V., Falco, M.D., Giaconia, A., Basile, A., Iaquaniello, G., 2012. Production of enriched methane by a molten-salt concentrated solar power plant coupled with a steam reforming process: An LCA study. Int. J. Hydrog. Energy 37 (15), 11556–11561.
Poling, B.E., Prausnitz, J.M., O'Connell, J.P., 2001. The Properties of Gases and Liquids, fifth ed. McGraw Hill, New York, USA.
Pushnov, A.S., 2006. Calculation of average bed porosity. Chem. Petrol. Eng. 42 (1–2), 14–17.
Qian, F., Sun, F., Du, W.L., Zhong, W.M., 2012. Novel hybrid evolutionary algorithm for dynamic optimization problems and its application in an ethylene oxide hydration reactor. Ind. Eng. Chem. Res. 51 (49), 15974–15985.
Roach, T.N.F., Salamon, P., Nulton, J., Andresen, B., Felts, B., Haas, A., Calhoun, S., Robinett, N., Rohwer, F., 2018. Application of finite-time and control thermodynamics to biological processes at multiple scales. J. Non-Equilibrum Thermodyn. 43 (3), 193–210.
Saidi, K., Hammami, S., 2015. The impact of CO_2 emissions and economic growth on energy consumption in 58 countries. Energy Rep. 1, 62–70.
Sauar, E., Kjelstrup, S., Lien, K., 1996. Equipartition of forces: a new principle for process design and optimization. Ind. Eng. Chem. Res. 35 (11), 4147–4153.
Schön, J.C., 2009. Finite-time thermodynamics and the optimal control of chemical syntheses. Z. Anorg. Allg. Chem. 635 (12), 1794–1806.
Sciazko, A., Komatsu, Y., Brus, G., Kimijima, S., Szmyd, J.S., 2014. A novel approach to improve the mathematical modelling of the internal reforming process for solid oxide fuel cells using the orthogonal least squares method. Int. J. Hydrog. Energy 39 (29), 16372–16389.
Shu, J., Grandjean, B.P.A., Kaliaguine, S., 1994. Methane steam reforming in asymmetric Pd- and Pd-Ag/porous SS membrane reactors. Appl. Catal. A 119 (2), 305–325.
Simpson, A., Lutz, A., 2007. Exergy analysis of hydrogen production via steam methane reforming. Int. J. Hydrog. Energy 32 (18), 4811–4820.
Tondeur, D., Kvaalen, E., 1987. Equipartition of entropy production. An optimality criterion for transfer and separation process. Ind. Eng. Chem. Res. 26 (1), 50–56.
Wang, C., Chen, L.G., Xia, S.J., Sun, F.R., 2016. Maximum production rate optimization for sulphuric acid decomposition process in tubular plug-flow reactor. Energy 99, 152–158.
Wesenberg, M.H., 2006. Gas Heated Steam Reformer Modelling (Ph. D. Thesis). Norwegian University of Science and Technology, Trondheim, Norway.
Wilhelmsen, Ø., Johannessen, E., Kjelstrup, S., 2010. Energy efficient reactor design simplified by second law analysis. Int. J. Hydrogen Energy 35 (24), 13219–13231.
Xu, J., Froment, G.F., 1989a. Methane steam reforming: II. Diffusional limitations and reactor simulation. AIChE J. 35 (1), 97–103.
Xu, J., Froment, G.F., 1989b. Methane steam reforming, methanation and water-gas shift: I. Intrinsic kinetics. AIChE J. 35 (1), 88–96.
Yagi, S., Kunii, D., 1957. Studies on effective thermal conductivities in packed beds. AIChE J. 3 (3), 373–381.
Yagi, S., Wakao, N., 1959. Heat and mass transfer from wall to fluid in packed beds. AIChE J. 5 (1), 79–85.
Yang, S.M., Tao, W.Q., 2006. Heat Transfer, fourth ed. Higher Education Press, Beijing, (in Chinese).
Yaws, C.L., 1999. Chemical Properties Handbook. McGraw-Hill, New York.
Zavoico, B.A., 2001. Solar Power Tower Design Basis Document, Revision 0. SAND2001-2100. Sandia National Laboratories, San Francisco, CA.
Zhang, L., Chen, L.G., Xia, S.J., Ge, Y.L., Wang, C., Feng, H.J., 2020. Multi-objective optimization for helium-heated reverse water gas shift reactor by using NSGA-II. Int. J. Heat Mass Transfer 148, 119025.
Zhang, L., Chen, L.G., Xia, S.J., Wang, C., Sun, F.R., 2018. Entropy generation minimization for reverse water gas shift (RWGS) reactor. Entropy 20 (6), 415.
Zhang, L., Xia, S.J., Chen, L.G., Ge, Y.L., Wang, C., Feng, H.J., 2019. Entropy generation rate minimization for hydrocarbon synthesis reactor from carbon dioxide and hydrogen. Int. J. Heat Mass Transfer 137, 1112–1123.
Zhou, Y., Zhao, C.Y., Liu, X.G., 2014. An iteratively adaptive particle swarm optimization approach for solving chemical dynamic optimization problems. CIESC J. 65 (4), 1296–1302, (in Chinese).